Chapter 1

Introduction

The hydrodynamic characteristics of most unmanned underwater vehicles (UUVs) are dominated by the body of the vehicle. These vehicles are designed to be approximately neutrally buoyant and manoeuvrability is provided by a combination of thrusters and control surfaces. The control surfaces are usually small compared to the body of the vehicle. These underwater vehicles may be classified into open frame vehicles and streamlined vehicles. Open frame UUVs are widely used in the offshore industry where modularity and low speed manoeuvrability are important. Streamlined vehicles are used extensively in naval and scientific applications were range, speed, efficiency and quiet operation are valuable in addition to low speed manoeuvrability.

The ability to accurately model the hydrodynamic characteristics of the streamlined type UUV body is important when accessing the performance of UUV designs. Historically, efforts to calculate the forces on buoyant vehicles immersed in fluid date back to the early part of the twentieth century with a focus on airships [1]. This early work was based on the assumption of inviscid, incompressible fluids and led to the creation of semi-empirical methods for calculating the forces on a body moving through a fluid. By the middle of the twentieth century these semi-empirical methods had been further developed to allow for viscosity and separation [2]. The development of the semi-empirical methods of calculating forces and moments experienced by vehicles moving through air was focussed towards the design of aeroplanes after the decline of the airship. The continued development of these methods for aircraft resulted in comprehensive methods such as the USAF DATCOM [3]. The techniques for calculating the hydrodynamic/aerodynamic coefficients were based on the body build-up method. This approach calculated the forces and moments due to individual components (fuselage, wings, tail, stores, etc) and then attempted to allow for the interactions between these components.

The methods developed for aircraft were applied to underwater vehicles in addition to

techniques developed for submersibles [4]. Peterson [5] evaluated seven methods of calculating the linear hydrodynamic coefficients on three torpedos and three submersibles. Peterson shows that the performance of these methods is variable and that it is important to understand that many of these methods were developed for a particular sort of body shape. The semi-empirical methods, despite their short comings continue to provide a valuable method for estimating the hydrodynamic coefficients [6] a long time after their initial development.

Increasing computational speed and memory capacity now allow for the application of Reynolds-Averaged Navier Stokes (RANS) equations to the calculation of the flow around UUV type shapes and the calculation of the resulting forces and moments. Some of the advantages of applying the RANS equations to determining the flow about such vehicles include:

- better allowance for interactions between body and fins.
- the prediction of flow structures around the body that may have important interactions with control surfaces or cause noise.
- an expected lower sensitivity to changes in body geometry than the semi-empirical methods and reduced sensitivity to the experimental data used in their development.

These must be weighed against the additional cost in time and computational resource associated with creating the required mesh and calculating the flow field.

Detailed in this document is the experimental testing of two idealised UUV bodies and the application of current CFD techniques to these idealised bodies. The ability of the selected CFD techniques to predicted the flow features observed and calculate the quantitative values measured during the testing of these idealised bodies is detailed.

Table 1.1 shows the dimensions and max length based Reynolds number (Re_l) of a range of military and research UUVs. The tabulated maximum Re_l values are quite high. Due to a requirement to maximise range, supply power to on board equipment, and drag cables (remotely operated vehicle, ROV) the Re_l at which UUVs function in day-to-day operation are often considerably less than the maxima.

Streamlined UUVs operating at Re_l below 4×10^6 are likely to have a considerable portion of their external surface with a laminar boundary layer. When these vehicles manoeuvre the regions of laminar, transitional and turbulent boundary layer will alter with the changing surface pressure distribution. The shift in transition when manoeuvring may well influence the hydrodynamic coefficients of the UUV. This means that the ability of the CFD techniques to handle a combination of laminar and turbulent flow may well be important if they are to suitably model the flow around typical UUV bodies.

PAP Mk 5 [7]	manufacturer	Société ECA
	length	$3.0\,m$
	diameter	$1.2\,m$
	height	$1.3\,m$
	length – diameter	$2.5-1$
	max velocity	$3.0\,ms^{-1}$
	max Re_l	9.0×10^6
Double Eagle Mk 2 [7]	manufacturer	Saab Bofors Dynamics AB
	length	$2.1\,m$
	width	$1.3\,m$
	height	$0.5\,m$
	length – width – height	$4.2-2.6-1$
	max velocity	$> 3.0\,ms^{-1}$
	max Re_l	$> 6.3\times10^6$
MARIUS [8]	length	$4.215\,m$
	width (of hull)	$1.1\,m$
	height	$0.6\,m$
	length – width – height	$7.0-1.8-1$
	max velocity	$2.0\,ms^{-1}$
	max Re_l	8.4×10^6
Wayamba [9]	manufacturer	DSTO
	length	$3.0\,m$
	width	$1.6\,m$
	height	$0.6\,m$
	length – width – height	$5.0-2.7-1$
	max velocity	$3.0\,ms^{-1}$
	max Re_l	9.0×10^6
AUV Testbed [10]	manufacturer	National Taiwan University
	length	$2.0\,m$
	width	$1.0\,m$
	height	$0.6\,m$
	length – width – height	$3.3-1.6-1$
	max velocity	$2.0\,ms^{-1}$
	max Re_l	4.0×10^6

Table 1.1: Specifications on a selection of UUVs

A considerable body of experimental and theoretical work has examined the flow around spheroids, as detailed in the literature review. Within this body of work there exists a particular interest in the 6–1 prolate spheroid. One of the motivations in the study of the 6–1 prolate spheroid has been due to its use as an idealised submarine shape. The 6–1 prolate spheroid in those studies often had the boundary layer tripped at 20% of its length.

An ellipsoid is a quadratic surfaces described in Cartesian coordinates (x_{bc}, y_{bc}, z_{bc}) by

$$\left(\frac{x_{bc}}{a_e}\right)^2 + \left(\frac{y_{bc}}{b_e}\right)^2 + \left(\frac{z_{bc}}{c_e}\right)^2 = 1 \tag{1.1}$$

where a_e, b_e, and c_e are constants. When two of these constants are equal the surface is categorised as a spheroid; if the two equal constants are less than the remaining constant the spheroid is designated as prolate. Only prolate spheroids were studied in the current investigation: they will simply be referred to as spheroids for the remainder of this thesis.

Ideally it would be possible to calculate the manoeuvring performance of a UUV given a specific set of thrust and control surface settings; mass distributions and hull geometry. This task would require accurate boundary layer transition and turbulence models; and appropriate meshing techniques. Currently the sort of computing power for this is not readily available nor could its expense be justified given the relatively low cost of UUVs. A less expensive option is to attempt to reproduce computationally the hydrodynamic testing currently performed to determine the hydrodynamic coefficients using a series of static and dynamic simulations. It should be noted that although this option is less expensive than the option presented previously it may well be more expensive than performing the actual testing.

For this application to be successful transition and turbulence models must exist that accurately determine regions of separated flow. It must be possible to test these models against suitable data sets. Chapters 3 to 8 detail a large number of measurements to enable such comparison.

The hydrodynamic testing detailed in this work was conducted at the Australian Maritime College (AMC) cavitation tunnel and examines flow around a 3–1 spheroid and a 4.2–2–1 ellipsoid. This investigation was the first sting-based testing conducted in this facility. Given this lack of previous testing, the 3–1 spheroid observation were undertaken to develop experience with suitable experimental techniques. The results obtained provided valuable experimental data that will be compared to previously published work on flow around spheroids. The 4.2–2–1 ellipsoidal body provides a suitable idealised shape for examining the flow around a flatfish type UUV.

Chapters 9 and 10 examine some comparisons between the measured and calculated flow around these generic UUV hulls using existing two-equation turbulence models. The experi-

mental data includes observations of boundary layer state allowing predetermined laminar and turbulent regions to be set in subsequent computational studies. This allows these numerical studies to avoid the difficulty of calculating the location of boundary layer transition.

Originally this project planned to conclude with an experimental and computational examination of the roll characteristics of the 4.2–2–1 ellipsoid. This was an area of interest as minimal information was available on non-axisymmetric hull shapes. In the case of flatfish type UUVs with their comparatively small control surfaces, the roll characteristics of the hull has an important influence on the manoeuvrability of the vehicle. However, as enough challenges were encountered in examining transcritical flow about the 3–1 spheroid and 4.2–2–1 ellipsoid this goal was not achieved.

Chapter 2

Literature Review

The experimental and theoretical examination of flow around spheroids has seen extensive study as this shape provides a logical step in complexity from axisymmetric flows when studied at zero incidences to complex three-dimensional flows at incidence. It has the additional advantage of having an elegant potential flow solution. Throughout the last century this shape has found significant practical application in the idealised study of flow past airships and submarines. The experimental testing and theoretical computations have developed in parallel: more detailed modelling has required greater knowledge of the flow for development and validation, and greater knowledge of the flow has identified deficiencies in the numerical techniques. Early work describing three-dimensional separated flow was performed by Legendre, this work is summarised by Délery [11] along with the experimental endeavours of Werlé who examined these flows over the same period.

2.1 Experimental Testing on Spheroids

Experimental testing on spheroids dates back to at least the early part of the twentieth century [12] when the influence of turbulence on such measurements was starting to be considered. In more recent times there have been two institutions (DFVLR-AVA, Göttingen and Virginia Polytechnic Institute and State University's Department of Aerospace and Ocean Engineering) conducting considerable research into the flow around ellipsoids in addition to numerous smaller endeavours.

2.1.1 Other Relevant Studies

Eichelbrenner's early work [13] measured the transition on a 6–1 spheroid using an evaporation technique with Kaolin at Re_l between 2×10^6 and 6×10^6. The results are compared the to those calculated using Michel's method with the application of the Mangler transformation. Good agreement is reported in axisymmetric flow. The differences at incidence are appreciable (10°). However, as noted by Cebeci and Cousteix [14], Michel's method is "strictly for two-dimensional incompressible flows on airfoils and are not applicable to two-dimensional flows with heating and suction and axisymmetric flows".

At the University of Iowa the flows over axisymmetric bodies have been studied experimentally and numerically. This work has included the examination of the flow over a 4.3–1 spheroid by Han and Patel [15] using dye injected from the model and wool tufts. The investigations focussed on the flow separation and were performed over a range of Re_l between 8×10^4 to 7×10^5 for angles of incidences, α, between 0° and 40°. The results were compared with the predictions of Wang (see section 2.2).

Fu et al. [16] examined the flow structure in the lee of a 6–1 spheroid at $\alpha = 10°$ and 20°. The tests were performed in the David Taylor Model Basin at Re_l between 0.42×10^6 and 2.1×10^6. The model used was $1.372\,m$ long and supported by a $50.8\,mm$ sting. Tests were performed with and without trip strips. The trip strip when used was placed at $x/l = 0.2$ and consisted of a $2\,mm$ diameter wire adhered to the surface. Particle displacement velocimetry (or particle image velocimetry, PIV) was used for taking slices of data, neutrally buoyant seed particles of $20-30\,\mu m$ diameter were used. The location of boundary layer separation was compared with results from VPI and DFVLR-AVA. The influence of the trip strip on the flow structures associated with the separation was examined, and the vorticity distribution at the most downstream slice was used to estimate force and moments.

2.1.2 DFVLR-AVA, Göttingen

The research at Göttingen has been performed as part of a long term project on "Three-dimensional Viscous Effects". Unless otherwise stated, the experimental research cited in this subsection has been conducted in Low Speed Wind Tunnel of the DFVLR-AVA. This facility has a $3\,m\times3\,m$ open test section with a maximum velocity of $62\,ms^{-1}$ and turbulence levels [17] of $0.1-0.2\%$. Kreplin et al. [18] detail the development of a 6–1 spheroid at DFVLR-AVA for use in this long term project. The 6–1 spheroid was $2.4\,m$ long, weighed $70\,kg$, and could be placed at a maximum angle of $\approx 30°$. The model was equipped with a traverse that allowed a probe to be accurately positioned with respect to the surface of the spheroid. The model could be rotated around its longitudinal axis to allow measurements around the body by a single set

of tappings or hot films. The model was reported as having vibrations at 6 Hz and 36 Hz. These vibrations were measured with accelerometers and dampened to some extent with shock absorbers. The deflection was reported as being 0.4 mm at the tip. The wall shear stress was measured with surface hot films. Boundary layer velocity distributions were determined using hot wire probes.

Meier et al. [17] examined the natural transition of the boundary layer and its separation on the spheroid detailed by Kreplin et al. [18]. The model had ten flush-mounted surface hot films coupled with twenty constant temperature anemometers. The time-mean measurements were performed by digital voltmeters, while the fluctuating measurements were conditioned by a 1 Hz-5 kHz bandpass filter. The measured voltages were used to calculate the wall shear stress. The magnitude and fluctuations of the wall shear stress were used to determine the state of the boundary layer. The model was rotated to allow measurements of the wall shear stress around the body. The wall shear stress on the body was measured for angles of attack at 0°, 2.5°, 10° and 30° for a range of Re_l from 3.2×10^6 to 9.6×10^6. The experimental results for laminar-turbulent transition with the model at 0° angle of attack compares favourably with calculations carried out by Cebeci [19] using linear stability theory.

Meier et al. [20] detail the three-dimensional boundary layer development and separation patterns on a body of revolution at incidence. The majority of the work used the 6–1 spheroid at DFVLR-AVA; the laminar testing was performed on a smaller 6–1 spheroid at $Re_l = 1.6 \times 10^6$. Measurements in the separated region were performed using a rotatable ten-hole probe. The use of the ten-hole probe allowed the velocity vector to be resolved in an arbitrary flow field. The velocity in the boundary layer was determined using a three-hole probe. The gradients of the surface pressure measurements for the laminar flow were compared to the potential flow calculations. From these comparisons the authors determine that there exist weak viscous-inviscid interactions. A similar comparison for the turbulent boundary layer shows strong viscous-inviscid interactions. Sketches of the flow topology in the separated region are provided and discussed along with vector maps of the velocity field at high angles of incidence (30°). The sketch of the flow field was produced with the aid of a laser sheet. One of the conclusions of the paper is that the flow topology for the case of a laminar boundary layer separating from the 6–1 spheroid inclined at 10° is similar to the topology of a turbulent boundary layer separating from the 6–1 spheroid inclined at 30°. The authors note the effect of gravity on their oil flow visualisation.

Vollmers et al. [21] discuss methods of identifying vortical flow features in three-dimensional flow. The data from the 6–1 spheroid [20] at 30° incidence were used to show the results of these flow identification techniques. The limitations of using surface pressure measurements to

determine flow separation are discussed. The authors state that surface pressure measurements tend only to pick up "massive separation".

Meier et al. [22] used a 6–1 spheroid to examine the influence of freestream turbulence on the boundary layer. This work involved the use of three large industrial wind tunnels in a number of configurations. Hot wire anemometers and microphones were used to measure the velocity and pressure fluctuations. The insensitivity of boundary layer stability to low frequency freestream turbulence was noted.

Kreplin and Stäger [23] measured the Reynolds shear stress components behind the 6–1 spheroid at the DFVLR-AVA. The 6–1 spheroid was placed at a 10° angle of incidence with a carborundum trip strip at $x/l = 0.2$. The shear stress measurements were performed using a four-wire probe. A three-hole pressure probe was used to determine the boundary layer displacement thickness. This paper examines how some of the assumptions in turbulence models compare with measured results. The Reynolds shear stress vector in the plane of the surface model does not align with the mean velocity gradient, so the authors note that isotropic turbulence models will not faithfully replicate flow conditions. The angle of the shear stress vector differs most from the angle of the velocity gradient vector at the outer edge of the boundary layer in the separated region. Plots of the anisotropy factor, $(\frac{v_{crossflow}}{v_{streamwise}})$, are provided. The Bradshaw (also known as Townsend) structural parameter for relating Reynolds shear stress to turbulent kinetic energy is displayed for a number of azimuthal angles.

2.1.3 Virginia Polytechnic Institute and State University

The research cited in this subsection was performed in the stability wind tunnel of the Department of Aerospace and Ocean Engineering at the Virginia Polytechnic Institute and State University (VPI) over the period 1992 to 1999. This wind tunnel has a working cross section of $1.83\,m \times 1.83\,m$ with a maximum velocity of $67\,m/s$. The test section is closed. The tunnel has a 9:1 contraction ratio and a turbulence level of approximately $0.03\% - 0.05\%$. New fan blades were fitted in 1996.

The 6–1 spheroid used for the testing at VPI was constructed from fibreglass and aluminium, it had a mass of $26.6\,kg$ and was $1.37\,m$ long. The model was mounted on a sting and comprised of five sections: nose, forward body, centre body, rear body, and tail. The forward and rear body were identical. A much lighter model of the same length was constructed for use when dynamic motion testing was performed [24].

Barber and Simpson [25] examined the Reynolds shear stress and boundary layer on the 6–1 spheroid placed at an incidence of 10°. The testing was performed at $Re_l = 4.0 \times 10^6$. Mean velocity and Reynolds shear stress measurements were obtained at two axial locations

(0.7 and 0.8 of full length). The near wake measurements of the velocity vector were performed using a United Sensor DC-125 3-D yaw head probe. A DANTEC 55P61 x-wire probe was used for Reynolds stress and velocity profile measurements. At each location the x-wire probe was rotated into six positions around its axis to get the Reynolds stresses. These measurements showed the turbulence was anisotropic in the regions measured. Values where calculated for the Townsend parameter (also known as the Bradshaw structural parameter [23]) from the measured data. The value of 0.15 used for the Townsend parameter in some one-equation turbulence models for two-dimensional flows is found to be "not wholly inaccurate" when applied to the boundary layer of the 6–1 spheroid. The value deviates from 0.15 as the distance from the wall is increased. (The results indicate that the use of this type of one-equation turbulence model in the near-wall region, $y^+ < 15$, is reasonable for the axial locations shown.) The characteristic mixing length in the regions measured tended to be less than the characteristic mixing length predicted for a two-dimensional boundary layer in the absence of a pressure gradient.

Ahn [26] in his thesis examines the flow about a 6–1 spheroid for Re_l ranging from 1.39×10^6 to 4.25×10^6. The spheroid was placed at angles of incidence up to 33°. Tests were performed with the boundary layer undergoing natural and forced transition. On body visualisation was performed using oil and surface mini-tufts. Measurements were made of the surface static and dynamic pressure. The RMS surface pressure fluctuation level was shown to increase at both separation and reattachment. Ahn found the "critical" Re_l for the 6–1 spheroid to be approximately 2.5×10^6.

Ahn also details the design of the internal force balance and a Dynamic Plunge-Pitch-Roll (DyPPiR) model support system. Measurements of force and moments on the body (except for drag) are presented. The internal balance had a calculated minimum natural frequency of 24 Hz when the model was attached. A 10 Hz filter was applied to the output of the force balance. No unsteady test measurements were detailed in the thesis.

Chesnakas and Simpson [27] detail the design of a miniature three component Laser Doppler Velocimeter (LDV) that was placed inside the 6–1 spheroid to measured the velocity profile through a thin flush-mounted window. The mounting of the LDV inside the body allows for short focal distances to the boundary layer and prevents movement of the spheroid relative to the LDV. The LDV was attached to a traverse that allowed it to be moved 50 mm in the radial and axial directions. The measurement volume had a diameter of 55 μm. The main source of error was noted to be due to the thermal expansion of the model; low data rates also prevented measurements closer than 0.1 mm to the wall. The measurements were performed with the spheroid at 10° incidence with $Re_l = 4.2 \times 10^6$. A trip strip was placed at 20% of the spheroid length. The maximum value for the normal stress at the given location was found to occur at

a y^+ value of 15. Measurements of the Reynolds shear stress showed the magnitude of $\overline{u'w'}$ to be significantly greater than $\overline{u'v'}$ very close to the wall.

Chesnakas and Simpson [28] used the previously detailed [27] facility, spheroid and fibre optic LDV to examine the components of the turbulent kinetic energy equation. The experiments were performed with the spheroid at 10° incidence for $Re_l = 4.20 \times 10^6$. Results are shown for the Reynolds stresses from one axial location, $x/l = 0.762$, at three circumferential angles near the separation line. The results show that near the separation line the maximum value for the normal stress at the given location occurred at a y^+ value of 12. The dominant Reynolds shear stress is measured to be $-\overline{u'v'}$; its measured value is close to its expected value of unity between $30 < y^+ < 300$ when normalised by the square of the friction velocity, u_τ. However some of the terms in the turbulent energy production equation that are normally ignored in the calculation of turbulent energy production are shown in this case to be significant at that location when y^+ is greater than 100. The authors note that the inequality between the flow gradient angle and the turbulent shear stress angle in the measured region will adversely affect the accuracy of turbulence models that assume an isotropic eddy viscosity. Also examined is the relative significance of diffusion, viscous diffusion and convection through the boundary layer near the separation line.

Chesnakas and Simpson [29], using the setup described in Chesnakas and Simpson [27], detail the existence of a trough of low velocity, low turbulence fluid behind the separation line. The experiments were performed at $Re_l = 4.20 \times 10^6$ with spheroid incidences of 10° and 20°. An array of techniques of determining the separation and reattachment line are examined; the use of oil flow techniques to determine flow angle are regarded favourably. The authors state that the assumption of isotropic eddy viscosity in highly three-dimensional flows is inappropriate.

Wetzel, Simpson and Cheesnakas [30] set out to provide a "definitive" paper on the precise measurement of cross-flow separation. The defining features of cross-flow separation are discussed, along with the difficulty in determining the starting point of such separations. Results from the 6–1 spheroid of DFVLR-AVA and VPI at incidences of 10° and greater are examined. The indicators of cross-flow separation and the measurements of these indicators are summarised as follows:

- *Converging Skin Friction Lines* are measured by oil flow patterns and hot films. Oil flow patterns tend to indicate separation further windward than other techniques; this error is attributed to gravity (not a problem if neutrally buoyant) or interactions between the oil and the flow. Hot films appear to provide accurate measurements; however, they require much effort to set up and perform best at high angles of incidence.

- *Zero crossflow velocity.* Near the wall the crossflow at separation is zero. This technique

requires measurements very close to the wall (LDV), and knowledge of the direction of the local separation (from oil flow), to determine the angle at which the flow must be zero.

- *Wall-normal velocity* is a maximum at separation. This again requires measurements of velocity very close to the wall but no knowledge of local flow direction, apart from normal to the surface. It is not a useful technique as the normal velocities close to the wall are very difficult to measure.
- *Skin friction magnitude* is a minimum near separation. This technique does not rely on an absolute value or require directional information. It provides good results with a closely packed grid of sensors.
- *Surface pressure* changes near cross-flow separation. Changes in C_p are not good indicators as C_p values are influenced by the entire flow field, and thus a poor indicator of local events. Although the pressure distribution tends to be flat in the separation region, it is difficult to determine where this flat region starts. C_p and $\partial C_p/\partial\varphi$ tend to have a minima leeward of separation. The pressure fluctuations exhibit a minimum at separation. These fluctuations appear to be a useful technique for determining separation if enough resolution is available.

Goody [31], as part of his thesis, examines the turbulent pressure fluctuations on the rear of the 6–1 spheroid at VPI. The experiments were performed with the spheroid at incidences of 10° and 20°. Correlations between the fluctuations in surface pressure and velocity components are examined. The pressure fluctuations at low angles of incidence are noted as being similar to that occurring in equilibrium flows. Regions of high wall shear stress are found to result in spectra with a larger high frequency component. Regions of reduced pressure fluctuations are noted to exist around separations, and local maxima in the pressure fluctuations at reattachment where flow with a high level of turbulence returns to the surface. The troughs of low energy fluid noted by Chesnakas and Simpson [29] are detailed in the figures.

Granlund [32] has examined steady and unsteady loadings (except drag) on three models, two of which had non-axisymmetric hulls, using the DyPPiR at VPI. The first model had its front and rear based on a 3.62–1.74–1 ellipsoid (length, width, height) with an added constant cross-section insert between the two halves of the same length as the combined nose and rear. The geometry of the second hull, the Newport News Experimental Model (NNEMO) is not available in open literature, but described as having a 6–2–1 length, width, height ratio. This work used a boundary layer trip placed at 5% of the models length. Wake surveys were performed by DeMoss [33] on NNEMO; these were used to determine the drag with and without the boundary layer trips.

2.2 Computational Fluid Dynamics on Spheroids

Elegant solutions for the potential flow around ellipsoids have been available since the late 1800s [34] and have found relevance in more recent publications [35][36]. The potential flow calculations have been used in the present work to generate surface pressure curves for comparison with measured curves for the model. This comparison provides a guide to the influence of boundary layer growth in regions where the flow is still relatively simple (no separation). Appendix A provides a detailed derivation.

The laminar and turbulent flow over a spheroid at incidence, using a previously determined pressure distribution, has been studied with the solution of the momentum and continuity equations for the boundary layer by numerous authors. Two of the larger bodies of work using this technique emanate from Wang or in conjunction with Cebeci. The laminar separation on a 4–1 spheroid at high and low incidence has been studied numerically by Wang [37][38]. The momentum and continuity equations for the boundary layer are solved over a large portion of the surface. The influence on the boundary layer velocity profile shape in the longitudinal direction due to flow reversal in azimuthal direction is examined along with the cross-flow's relevance to separation. The types of separation are also classified. Patel and Choi [39] confirmed some of Wang's calculations for laminar separated flow from the 4–1 spheroid at low incidence (6°). They compared two different numerical techniques using potential theory to supply the required pressure distribution for the spheroid. On a second elongated body of revolution at incidence experimental pressure measurements were used to supply the pressure distribution; comparisons between the measured and potential pressure distributions for this body are close over the front half of the body but generally poor towards the rear.

Cebeci in collaboration with others has performed extensive numerical studies on three-dimensional boundary layers using, for the most part, meshes based on a body fixed coordinate system. The method used calculated the boundary layer velocity from a predetermined pressure field. The pressure field was determined from potential flow calculations or experimental data. A portion of this work was focussed on the flow around the 6–1 spheroid. This work examined a number of areas including the numerical difficulties associated with flow reversal, separation and the singularity at the forward stagnation point [40][41]. Cebeci [42] also calculated boundary layer transition on the spheroid at incidence using the linear stability e^n method; the results were compared with the experimental data of Meier and Kreplin [17]. Patel and Baek [43] have used similar numerical techniques to study the flow around a 6–1 spheroid at 10° incidence using both potential and measured pressure fields. The studies examined one case of laminar flow, and one with laminar, transitional and turbulent flow.

The parabolised Navier–Stokes equations have been used by Rosenfeld et al. [44] to examine

the laminar flow around a 4–1 and 6–1 spheroid at incidence for Re_l of around 10^6. This method does not require the use of a predetermined pressure distribution and allows calculations in regions of separated flow. The flow field was calculated for the centre 80% of the body and the resulting skin friction compared to experimental and computed results. Later work [45] examined the surface pressure and off-body flow.

The flow about a 6–1 spheroid at high α and Re_l, of 30° and 7.2×10^6 respectively, was used by Gee et al. [46] to study the performance of two algebraic turbulence models with two additional modifications. A finite difference scheme was used to solve the RANS equations for the mesh over the entire spheroid and sting. The surface flow and surface pressure was compared to the experimental results of Meier and Kreplin [17]. Two of the five models showed discrepancies due to the incorrect calculation of the turbulent viscosity. This resulted from vortical structures in the separated flow. The remaining models were able to determine the primary and secondary separation lines.

Constantinescu et al. [47] used a Detached-Eddy Simulation (DES) and a RANS simulation to calculate the flow around a 6–1 prolate spheroid at 10° and 20° incidence for $Re_l = 4.2 \times 10^6$. The DES calculation used a Spalart-Allmaras turbulence model close to the wall; the RANS calculations used a Spalart-Allmaras turbulence model, and also tested separately a correction to this model to allow for anisotropy of the Reynolds Stress and a modified turbulent viscosity to account for streamline curvature. The turbulence model was switched on at 20% of the body length in order to match the trip position of Chesnakas and Simpson [29], whose experimental results are compared with these computations. The authors conclude that there is no significant difference in the mean quantities predicted for these two cases by the DES and RANS calculation (or its modifications).

Kim et al. [48] evaluate the performance of the Spalart-Allmaras, Shear Stress Transport (SST), two variants of the k–ω model, and three variants of Reynolds Stress turbulence models, against measurements of the 6–1 spheroid performed at VPI. The comparisons are performed at a high angles of incidence, 10° through 30°, with the majority of results presented for 20°. The calculations were performed with the turbulence models being switched on at 20% of the body length. The k–ω model of Wilcox [49] with a low Reynolds number correction is reported to have the best performance of the eddy viscosity turbulence models. The use of wall elements was determined to provide similar results to modelling through to the viscous sublayer.

Wikström et al. [50] compare results from Large Eddy Simulation (LES) on a 6–1 spheroid at incidences of 10° and 20° to results from VPI. The LES was performed with different subgrid models, with and without wall modelling. This work concludes that improved near-wall modelling is required. Karlsson and Fureby [51] have compared results from numerical studies of the

6–1 spheroid using the Spalart-Allmaras turbulence model, DES and LES to the measurements obtained at VPI. This paper examined the influence of modelling the trip strip by increasing the subgrid viscosity and of using different techniques to determine the subgrid length scale for the LES. The authors report favourably on the results from the DES. LES showed some success, but displayed sensitivity to the subgrid scale and the simulated trip.

2.3 Summary

The preceeding sections of this chapter highlight some of the experimental and computational studies that have been performed almost entirely on axisymmetric shaped bodies. A large proportion of these studies examined the flow around one shape, the 6–1 prolate spheroid, which is of interest as a generic submarine body. Although some of the computational work has allowed for natural transition the more recent work using finite volume codes tends not to focus on this aspect. This is reasonable if the flows of ultimate application are predominately turbulent. Additionally a considerable segment of this work has been studying flow at moderate to high incidence. The following chapters provide original experimental data on bodies with a lower aspect ratio and include a generic non-axisymmetric hull shape. This data is measured over a range of Reynolds numbers and incidences applicable to the every day operation of streamlined UUVs; and in the majority of cases boundary layer transition is not forced. Later chapters compare the predictions of some two-equation turbulence models with measured data. The turbulence models were modified to allow for the measured laminar regions.

Chapter 3

General Experimental Setup

3.1 Cavitation Tunnel

The tests were performed in the AMC Tom Fink Cavitation Tunnel. This is a closed circuit water tunnel facility with a nominal test section of $0.6\,m \times 0.6\,m \times 2.6\,m$, a velocity range from $2\,ms^{-1}$ to $12\,ms^{-1}$, a pressure range of $4\,kPa$ to $400\,kPa$ on the test section centreline and a freestream turbulence intensity of approximately 0.5% [52]. A turbulent length scale of $27\,mm$ was estimated from the integration, with respect to time, of the auto-correlation coefficient of hot film data measuring the streamwise velocity. The sides of the test section are parallel; the top is horizontal. The bottom slopes at 0.44° from horizontal giving an increase in test section height from $600\,mm$ at entry to $620\,mm$ at exit; this is designed to compensate for boundary layer growth and keep the core velocity and static pressure nearly constant through the test section. The slope on the bottom surface results in angle of about 0.2° in the core flow, measured from the top surface.

The primary material used in the construction of the facility is 304 stainless steel; all areas exposed to water except the windows are built using this material. The test section has three acrylic windows on each side of the test section and two acrylic windows along the bottom. These windows have a high quality finish. The models are mounted from the top on a stainless steel window $1620\,mm \times 380\,mm$. The models may be mounted $\pm 750\,mm$ in the streamwise direction from the centre of the test section in $150mm$ intervals (positive downstream of centre). All the testing performed was conducted with the model centre within $150mm$ of the test section centre in the streamwise direction.

The tunnel velocity and pressure are set manually and maintained by a PID controller. Data acquisition was performed using a PC fitted with the National Instruments PCI–4472 card. This card provides eight channels each with a 24 bit ADC with a maximum sample rate

of $102.4\,kHz$. Labview software was written to automate the data acquisition where practical.

The Cartesian coordinate system for the tunnel has its vertical axis, z_t normal to the horizontal top surface of the test section; the transverse axis y_t is normal to the sides of the test section; and the longitudinal axis x_t is parallel to the top window with its positive coordinates in the downstream direction. The origin is located in the centre of the test section in the x_t and y_t direction, and $300\,mm$ below the top surface of the test section in the z_t direction.

3.2 Support Foil

The support foil was mounted to the top window of the tunnel via a $220\,mm$ flange and was aligned with the flow using dowels. A symmetrical NACA 5-digit 16-series foil shape was selected with a $140\,mm$ chord and $40\,mm$ maximum thickness. This provided a thickness-to-chord ratio close to the optimum suggested by Hoerner [53] to minimise non-dimensional drag, C_D, (based on frontal area) for a two-dimensional strut. The foil was constructed from cast stainless steel; the casting facilitates the placement of a $60\,mm \times 16\,mm$ hole through the centre of the foil in the span-wise direction to reduce mass and accommodate cabling and tubes. A $80\,mm \times 16\,mm$ recess $22\,mm$ deep was machined into the bottom of the foil; a matching stub was machined onto the foil section of the sting to provide precise location and rigid mounting for the sting. Two M6 screws tightened wedges that locked the sting to the foil. The centre of the sting, when mounted to the foil, was equidistant from each side and $300\,mm$ from the top of the test section.

3.3 3–1 Spheroid Model

The 3–1 spheroid model was designed for measurements of surface pressure, boundary layer state, force and flow visualisation. The angle of incidence, α, of the spheroid may be altered between $\pm 10°$ in $2°$ increments by switching an internal angle bracket. The centre of rotation when the incidence is adjusted is located where the sting enters the model, $161\,mm$ behind the centre of the model. With the $0°$ internal support in place the major axis of the prolate spheroid model is parallel with the top of the test section and thus aligned at $\alpha = -0.2°$ to the streamwise direction of the test section flow. The shell may be rotated around the major axis of the spheroid on the central boss in the azimuthal direction, φ, at $15°$ degree intervals. Fig. 3.1 provides an exploded view of the model; the model coordinate system is shown in Fig. 3.2.

The front and rear shell of the model were manufactured from PVC plastic. PVC was selected due to its low density, negligible absorption of water, suitability for use with a broad range of adhesives, and ability to be finished to a smooth surface. A grid was placed on the

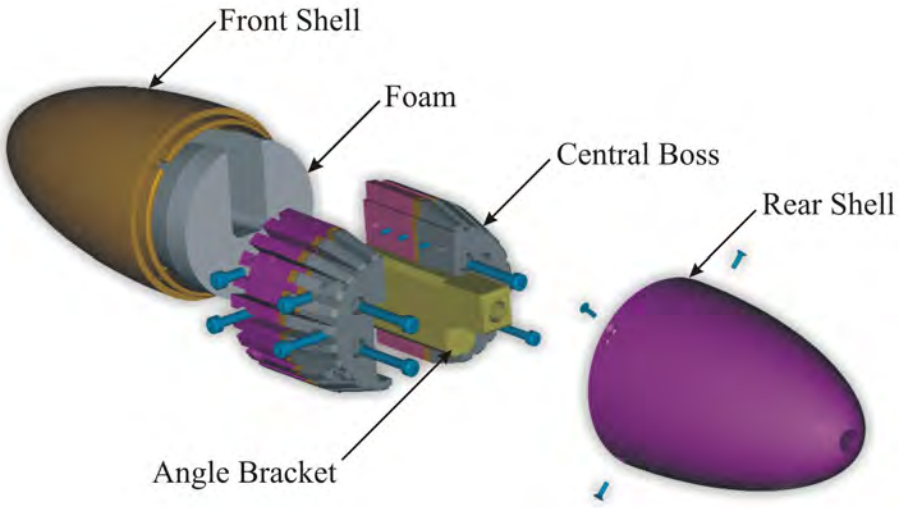

Figure 3.1: Exploded View of 3–1 Spheroid Model

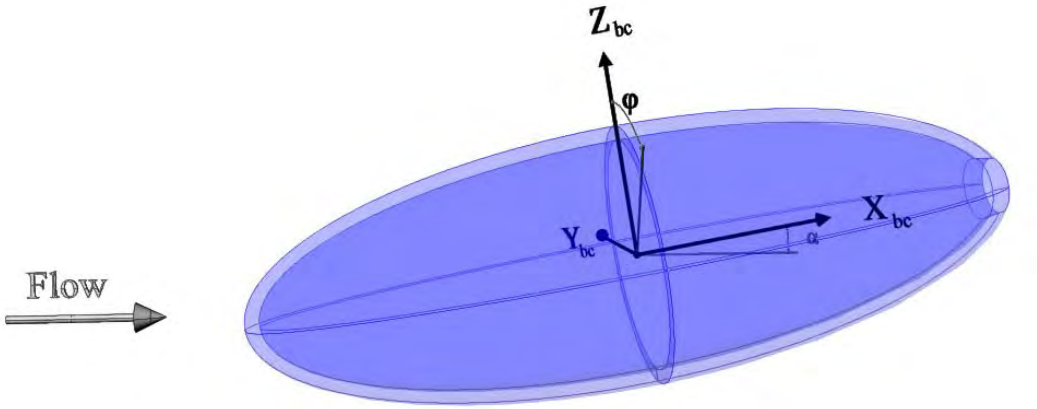

Figure 3.2: Coordinate system for 3–1 spheroid model

model to facilitate flow visualisation. The front and rear shell were machined $1\,mm$ oversize and $2\,mm$ deep grooves were then machined at the appropriate positions and filled with a coloured epoxy adhesive. After the adhesive had cured the shell was machined to its final dimensions. This technique provided a surface that was smooth with no discernible discontinuity to the fingertips. The model has a nominal length, l, of $330\,mm$, with $4\,mm$ truncated from the rear in order to provide access for the sting. To minimise the in-water mass of the model the void inside the front shell was filled with closed cell foam (Divinycell$^{\mathrm{TM}}$).

The sting for the spheroid positioned the centre of the model, when $\alpha = -0.2°$, $285\,mm$ in front of the leading edge of the foil support. At the foil the sting has a diameter of $40\,mm$ and transitions to a $23\,mm$ diameter approximately $35\,mm$ before entering the spheroid. The transition is obtained using the odd components of a fifth order polynomial to provide a smooth pressure gradient, and occurs between $10\,mm$ and $90\,mm$ upstream of the leading edge of the

foil. The sting has a $9.5\,mm$ axial hole through the centre to allow access for cables and tubes. Bungs were used to seal the cables etc., or the block the hole when not in use to prevent flow between the interior of the spheroid and the foil.

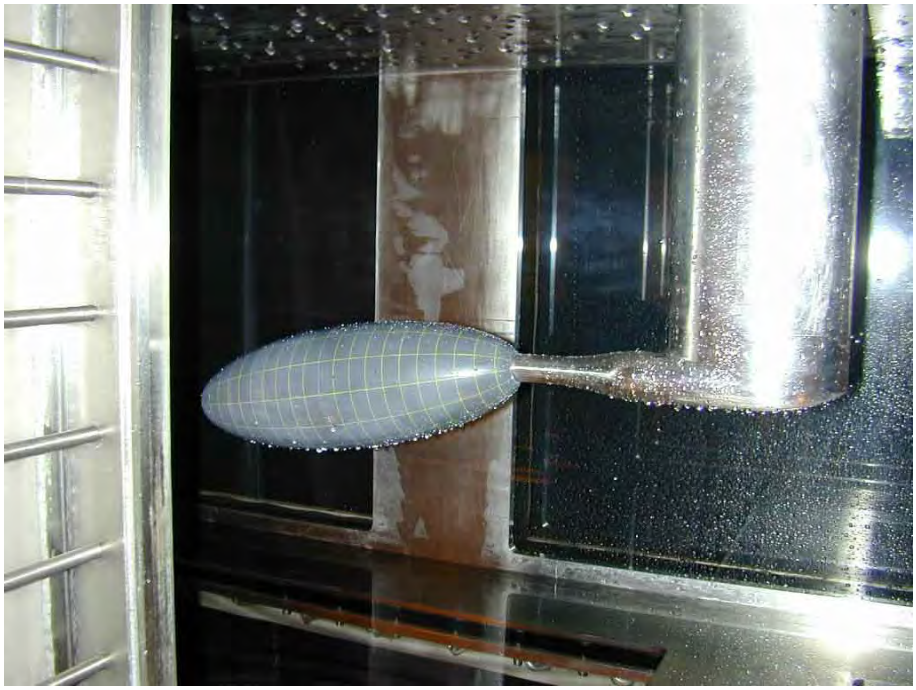

Figure 3.3: 3–1 Spheroid Model in Test Section

3.4 Vibration of 3–1 Spheroid Model

One of the criteria in designing the model was to maximise the natural vibration frequency, as the motion of the structure may have an influence on the flow. This is achieved by minimising the mass of the model and supports while maximising the stiffness. Items that need to be considered in the design include:

- Even if the model is massless the added mass in the lateral direction due to the displaced water is significant ($\approx 0.8\ \rho_W V_e$ [54] for a 3–1 spheroid where V_e is the volume of the spheroid and ρ_W the density of water). This results in a limit, based on the volume, which can be achieved for the apparent mass of the model.

- Decreasing the length of the sting increases the stiffness, but increases the interference caused by the support foil.

- Increasing the diameter of the sting increases the stiffness, but increases the influence the sting has on the flow around the model.

- Selection of the materials for the sting and foil play an important role, with high elastic modulus and low density desirable. The material must also be compatible with the rest of the tunnel structure.

The chosen design resulted in a compromise that aimed to keep the first natural frequency above $50\,Hz$ while minimising the influence of the support structures. The most flexible element in the final design was the sting. Minimising the torsion and bending of the foil resulted in a relatively thick support foil.

Given the mass of the spheroid and the added mass of all the components, the process of material selection for the support foil and sting is more involved than just selecting the material with the greatest stiffness-to-density ratio. The high elastic modulus of stainless steel and its compatibility with the rest of the tunnel structure resulted in its selection for the foil and sting. Other less noble materials tend to act as sacrificial anodes with the large area of stainless present in the tunnel (although this problem is reduced with the more recent use of demineralised water in the circuit).

Measurements on the model showed the first natural frequency occurred at $44\,Hz$ with the maximum amplitude of the displacement ranging from $5\,\mu m$ at $Re_l = 1.0 \times 10^6$ to $80\,\mu m$ at $Re_l = 4.0 \times 10^6$. The frequency response of the spheroid at $\alpha = -10.2°$ is shown for these two values of Re_l in Fig. 3.4. As the sting is axisymmetric, the influence of the torsion of the support foil is evident from the lower natural frequency and greater amplitude of the vibration in the horizontal direction compared with the corresponding values in the vertical direction.

3.5 4.2–2–1 Ellipsoid Model

The major axis has a length of $165\,mm$; minor axes in the y_{bc} and z_{bc} directions have lengths of $55\sqrt{2}$ and $55/\sqrt{2}$ respectively. At $\alpha = -0.2°$ the x_{bc}–y_{bc} plane is parallel to the top window. The cross sectional area in the y_{bc}–z_{bc} plane for the 4.2–2–1 ellipsoid is identical to that of the 3–1 spheroid at the same x_{bc}.

Three models with identical exteriors were manufactured: one for surface pressure measurements; one for force measurements; and a general purpose model for boundary layer and wake surveys. The internal structure for the general purpose and surface pressure models were for practical purposes identical and is shown in Fig. 3.5. The model for the force measurements

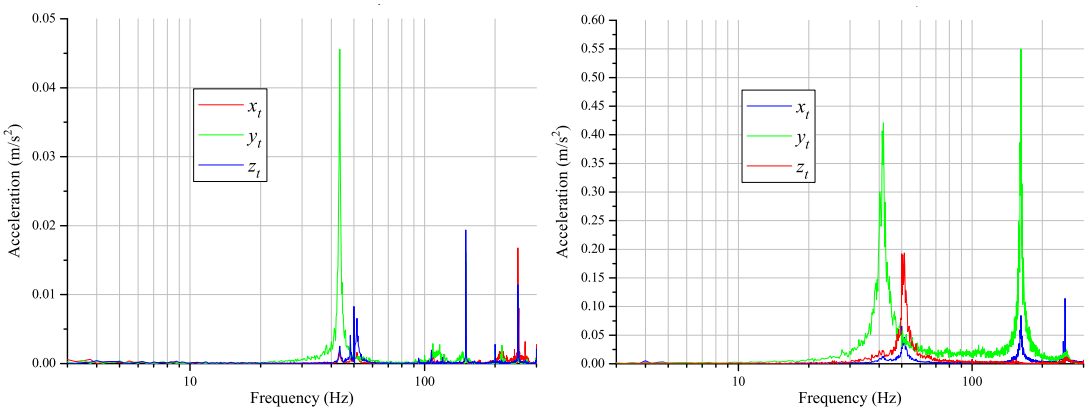

(a) $Re_l = 1.0 \times 10^6$ (b) $Re_l = 4.0 \times 10^6$

Figure 3.4: Vibration of spheroid model at $\alpha = -10.2°$. Spikes at 50 Hz and harmonics of 50 Hz are due to electrical power supply interference.

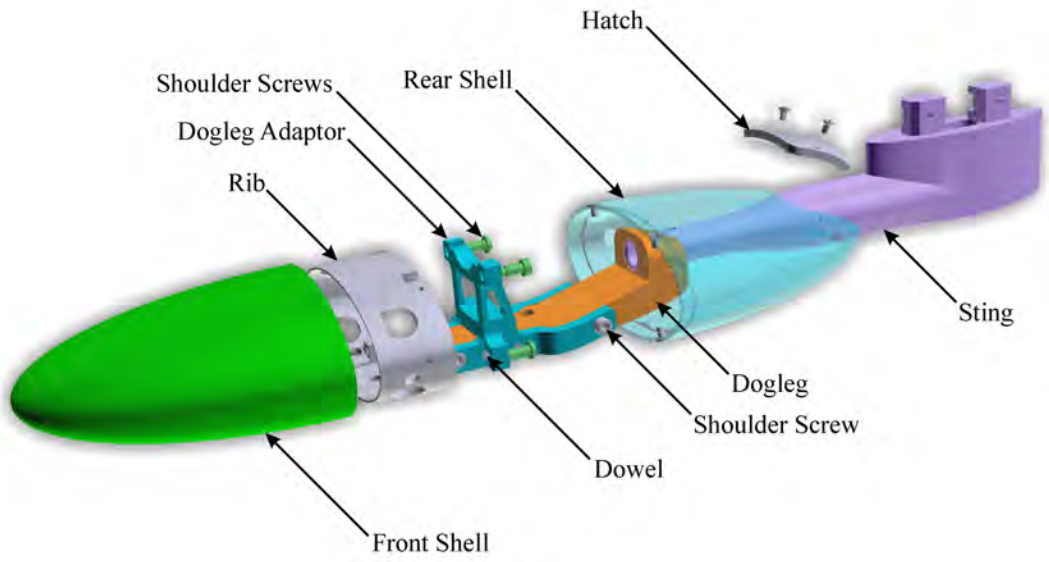

Figure 3.5: Exploded View of 4.2–2–1 Spheroid Model

was designed to accommodate an internal force balance. The front and rear shells for all models were constructed from PVC with a stainless steel rib inserted to provide one or more mounting points and added stiffness. The rib was pinned and glued to the front shell. The incidence of the model was altered through the use of dogleg supports which rotated the model normal to x_t axis (for the majority of tests about y_t) at $x_{bc} = -161\,mm$. Three dogleg supports were manufactured with 0°, 6°, and 10° angles to the sting. The dogleg supports were shaped to provide the maximum room for the internal force balance. Accommodating the internal force balance also resulted in a sting that terminated shortly after entering the rear shell of the ellipsoid. The end of the sting was tapered with a 9° included angle; a matching tapered hole

on the dogleg support provided a rigid connection; and axial alignment was provided by a key. A hole through the centre of the sting provided access from the foil; this was sealed to prevent uncontrolled flow. A removable hatch on the rear shell allowed this part to be slid back along the thickened sting to facilitate the fitting of the model with its internals. The joins between the shells and between the rear shell and hatch were sealed with a setting silicone compound before testing. The screws holding these sections were machined flush, sealed and smoothed before testing.

The stiffness of the sting was increased from that used with the 3–1 spheroid to allow for the extra mass of the internal balance when it was required. This sting employed the same fifth order diameter variation as the sting used with the 3–1 spheroid but this started $30\,mm$ upstream creating a longer section at $40\,mm$ diameter; the section at a diameter of $23\,mm$ was reduced by a similar quantity. The sting and dogleg brackets placed the centre of the model approximately $280\,mm$ in front of the leading edge of the support foil. The back half of the foil section of the sting was also modified, as testing with the 3–1 spheroid had shown that the flow from the underside of the sting was being given a vertical component. The modifications showed in Fig. 3.6 were designed to reduce this vertical component, even though it was not expected to have a measurable influence on the results.

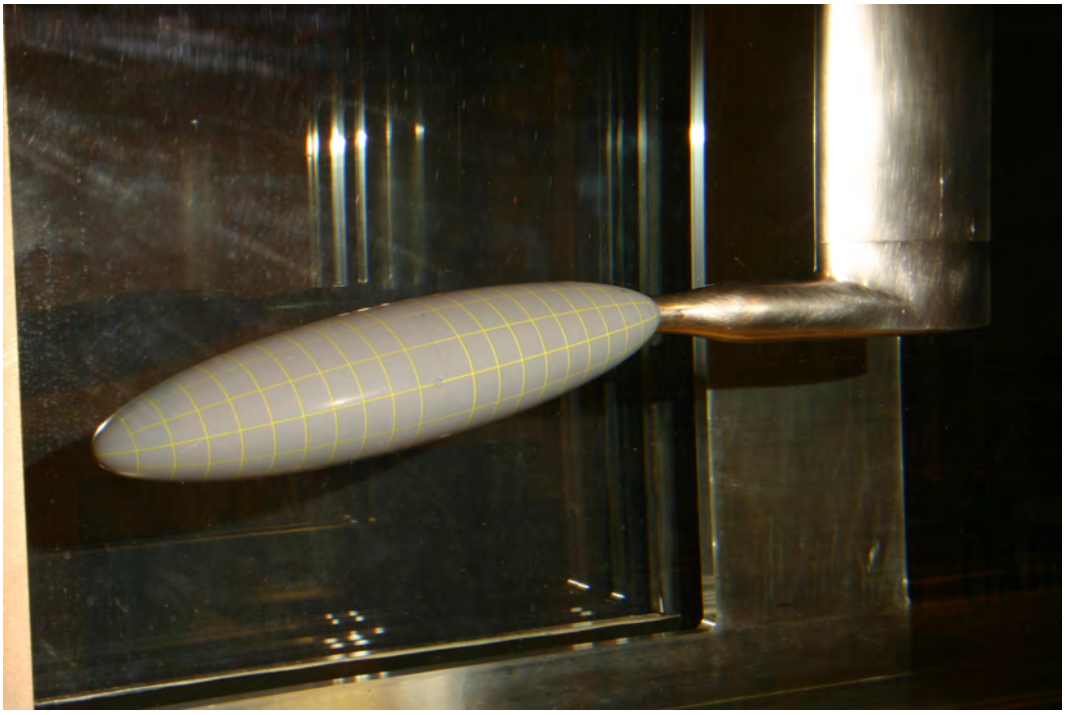

Figure 3.6: 4.2–2–1 Ellipsoid Model in Test Section

3.6 Vibration of 4.2–2–1 Ellipsoid Model

The structural design of the 4.2–2–1 ellipsoid required consideration of the same issues as the spheroid, with the additional complication of allowing for the inclusion of an internal force balance and the desire to reuse the majority of components when force measurements were not required. The relative shifts of natural frequencies in the y_t and z_t direction compared to the 3–1 spheroid are consistent with the decrease and increase in added mass of the ellipsoid in the y_{bc} and z_{bc} directions, respectively. The frequency response without the internal force balance installed is shown in Fig. 3.7.

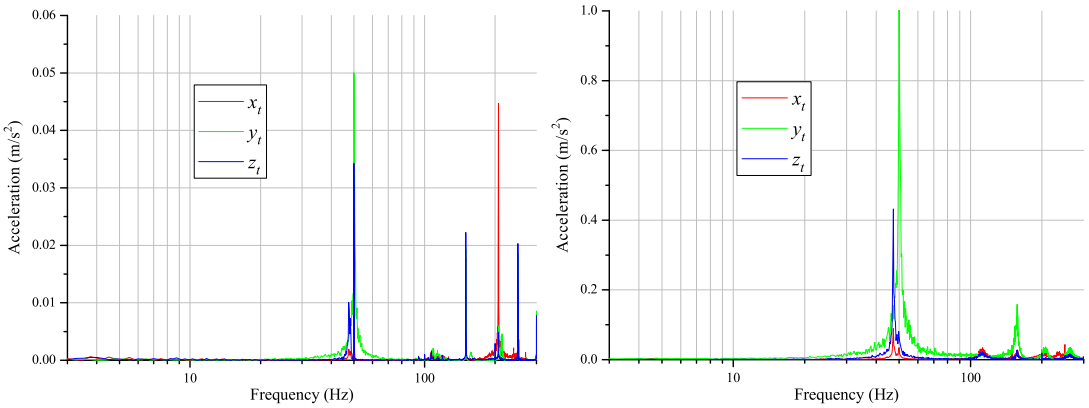

(a) $Re_l = 1.0 \times 10^6$ (b) $Re_l = 4.0 \times 10^6$

Figure 3.7: Vibration of ellipsoid model at $\alpha = -10.2°$. Spikes at 50 Hz and harmonics of 50 Hz due to electrical power supply interference.